Bone Quality Assessment at the Atomic Scale

J. M. D. A. Rollo, R. S. Boffa, R. Cesar, R. Erbereli, D. C. Schwab and T. P. Leivas

Abstract The assessment of osteoporosis regarding bone mass and microarchitecture "quality" contributes in determining fracture risk. Therefore, the crystalline structure of hydroxyapatite may indicate the quality of trabecular bones through the identification of crystallite sizes, microhardness and microdeformation values and calcium and phosphorous proportions in the three types of bones: normal, osteopenic, and osteoporotic. Nine L1 vertebrae-dried trabecular bones from human cadavers were used. The characterization of the three types of bones was made through scanning electron microscopy, EDS, microhardness, and X-ray diffractometry with the

J. M. D. A. Rollo (✉) · R. S. Boffa
Departamento de Engenharia de Materiais, Universidade de São Paulo (USP), Escola de Engenharia de São Carlos, Av. Trabalhador Saocarlense, 400—Parque Arnold Schimidt, 13565-590 São Carlos, SP, Brazil
e-mail: tfase@sc.usp.br

R. S. Boffa
e-mail: boffa3266@hotmail.com

R. Cesar · R. Erbereli
Departamento de Engenharia Mecânica, Universidade de São Paulo (USP), Escola de Engenharia de São Carlos, Av. Trabalhador Saocarlense, 400 – Parque Arnold Schimidt, 13565-590 São Carlos, SP, Brazil
e-mail: reinaldofisica@gmail.com

R. Erbereli
e-mail: rogerio.erbereli@usp.br

D. C. Schwab
DCS - English Consultancy Services, Rua São Sebastião, 1795 – Sala 7, 13560-230 São Carlos, Brazil
e-mail: dcschwab@gmail.com

T. P. Leivas
Instituto de Ortopedia E Traumatologia, HCFMUSP-OIT—Hospital de Clinicas da Faculdade de Medicina, Universidade de São Paulo (USP), Rua Dr. Ovidio Pires de Campos, 333 – Cerqueira Cesar, 05403-010 São Paulo, Brazil
e-mail: tomazpuga@gmail.com

J. Belinha et al. (eds.), *The Computational Mechanics of Bone Tissue*,
Lecture Notes in Computational Vision and Biomechanics 35,
https://doi.org/10.1007/978-3-030-37541-6_2

Rietveld refinement method. The results show that the microstructural characterization possibilities the identification of the three types of bones: normal, osteopenic, and osteoporotic, allowing the detection of osteoporosis based on bone quality.

1 Introduction

Osteoporosis is defined by the National Institutes of Health as a skeleton disorder characterized by compromised bone resistance and high fracture risk [1].

Professionals have assumed that all patients with very low T-scores (bone mass measurement) have osteoporosis. Values higher than −1.0 are considered normal, between −1.0 and −2.5 osteopenic and below −2.5 osteoporotic. However, the T-score derives from a specific population; therefore, in other populations, the T-score has its problems. Since the bone mineral density (BMD) is a limited fracture risk indicator, the clinical and scientific interest has increased in the complementary analysis that could improve the fracture risk prediction [2–6].

A normal BMD does not guarantee that a fracture will not happen and, reciprocally, for a BMD in the osteoporotic level, fractures will be more probable, but not impossible to prevent. Due to these paradoxes in treatment, the term became popular in the early nineties and, since then, the concept of bone resistance amplified to more than just density, also aggregating characteristics related to bone quality. There are many properties representing bone quality, among them there is the crystalline structure of the inorganic part of the bone (hydroxyapatite crystals) [1, 7–17].

Analyzing the crystalline structure in the atomic scale (crystallite size, calcium and phosphorous parts, microdeformation), visually (scanning electron microscopy), and mechanically (microhardness), it is expected to identify relations, for dried trabecular bones indicating their condition regarding bone quality.

Even though it is not satisfactory, the evaluation for osteoporosis considers only bone quantity (BMD). It is important to evaluate bone quality with the analysis of the inorganic part of the bone through the microstructural characterization of hydroxyapatite crystals.

2 Hydroxyapatite

Biological hydroxyapatite (HA) is considered the structural model for the mineral phase of the bone, and it presents imperfections, different from the HA found in rocks. The ions on the crystal surface are hydrated, generating a layer of ions and water called hydration cover, which facilitates the exchange of ions between the crystal and the interstitial fluid. It may have multiple substitutions and deficiencies in all ionic sites. Among the impurities of the apatite crystals, the most noticeable is

the replacement of B type carbonates from the HA (CHA) in the phosphates groups, also presenting replacements of potassium, magnesium, strontium and sodium for calcium ions, chlorides and fluorides for the hydroxyl groups. These impurities may alter the crystalline structure, reducing the crystallinity, affecting the elasticity and the bone resistance of the apatite. The size of the crystal and the bone mineral crystallinity may also be altered due to certain diseases and therapies [18–28].

Therefore, the HA may have a varied composition. Calcium-deficient hydroxyapatite (CDHA), or non-stoichiometric, can be obtained in low temperatures, with a composition expressed as $Ca_{10-x}(HPO_4)_x(PO_4)_{6-x}(OH)_{2-x}$, where x varies from 0 to 1: 0 for non-stoichiometric HA and 1 for complete CDHA [29]

Pure HA presents a molar reason of 1.67, as shown in Table 1.

Table 1 Main calcium phosphates

Name	Formula	Ca/P	Mineral	Symbol
Monocalcium phosphate monohydrate	$Ca(H_2PO_4)_2 \cdot H_2O$	0.50	–	MCPM
Dicalcium phosphate	$CaHPO_4$	1.00	Monetite	DCP
Dicalcium phosphate dihydrate	$CaHPO_4 \cdot 2H_2O$	1.00	Brushite	DCPD
Octacalcium phospate	$Ca_8H_2(PO_4)_6 \cdot 5H_2O$	1.33	–	OCP
Precipitated hydroxyapatite	$Ca_{10-x}(HPO_4)_x(PO_4)_{6-x}(OH)_{2-x}$	1.50–1.67	–	PHA
Tricalcium phosphate	$Ca_9(HPO_4)(PO_4)_5(OH)$	1.5	–	TCP
Amorphous calcium phosphate	$Ca_3(PO_4)_2 \cdot nH_2O$[a]	1.5	–	ACP
Monocalcium phosphate	$Ca(H_2PO_4)_2$	0.50	–	MCP
α—Tricalcium phosphate	α-$Ca_3(PO_4)_2$	1.5	–	α-TCP
β—Tricalcium phosphate	β-$Ca_3(PO_4)_2$	1.50	–	β–TCP
Sintered hydroxyapatite	$Ca_5(PO_4)_3OH$	1.67	Hydroxyapatite	HA
Oxyapatite	$Ca_{10}(PO_4)_6O$	1.67	–	OXA
Tetracalcium phosphate	$Ca_4(PO_4)_2O$	2.00	Hilgenstockite	TetCP
Carbonated apatite	$Ca_{8.8}(HPO_4)_{0.7}(PO_4)_{4.5}(CO_3)_{0.7}(OH)_{1.3}$		Dahlite	CAP

The higher the molar reason Ca/P, the lower will be the solubility of the material, but this rate is also influenced regarding its chemical composition, local pH, temperature, particle sizes, and crystallinity [30–33].

3 Rietveld Refinement Method

The X-ray diffraction characterization methods are used for the indexation of the crystalline phases, unit cell refinement, crystallite size determination, net microdeformation, quantitative analysis of the phases, etc. [34, 35].

The structure of a typical diffraction standard in the powder can be described by the positions, intensities, and forms of the multiple Bragg reflections. Each of these components holds information about the crystalline structure of the material, sample properties, and the instrumental standards, as seen in Table 2 [36].

The size of the crystallite and the residual tension (microdeformations) may then be analyzed by the format of the peak, more specifically by its width, also taking into consideration the instrumental nature and the specific conditions for each experiment (diffractometer slot width, band wavelength generated by the source, angular divergence of the beams, etc.) [36].

Once a routine is established for the calculus of the profile, it is necessary to choose the refinement method to be adopted. The most commonly accepted strategy is the minimum squares technique, which aims to minimize the sum of the squares of the differences between the theoretical model and the data obtained in the measurements, adjusting values of the parameters present in the theory in order to find the ideal values for these parameters.

In 1967–69, Rietveld presented a refinement method of crystalline structures. The Rietveld method is a powerful tool for the structural analysis of most crystalline materials in powder form, which is used nowadays to solve all problems mentioned before (unit cell refinement, crystallite size determination, net microdeformation, quantitative analysis of the phases) using the minimum squares technique. For its application, the diffraction data is used as it lefts the diffractometer, without any sort

Table 2 Possible information to be analyzed by the X-ray generated diffractogram [36]

Standard component	Crystalline structure	Specimen property	Instrumental parameter
Peak position	Unitary cell parameters	Absorption; porosity	Radiation (wavelength); sample alignment
Peak intensity	Atomic parameters	Preferred orientation; Absorption; porosity	Geometry and configuration
Peak format	Crystallinity; disarray; defects	Crystallite size; tension	X-ray conditioning

of alteration, which follows the scientific criteria that no modifications must be done to the observations for them to be analyzed [37, 38].

At first, the method was only applied in materials analyzed by neutrons diffraction. Later on, after some adaptations, its application was made possible for measures obtained by X-ray diffraction as well. For the X-ray, there are no simple functions, different from the neutrons, the radiation with which the method was originally developed has peaks modeled by Gaussian. The peaks are closer to Gaussian for small spreading angles and closer to Lorentzian for large angles. Therefore, the pseudo-Voigt function is used, a normalized linear combination of a Gaussian with a Lorentzian as shown in Eq. (1): [39–42].

$$pV(x) = \eta L(X) + (1 - \eta)G(X) \tag{1}$$

where η is a refined parameter that determines the percentage of contribution of each function; L is the Lorentzian; G the Gaussian function; $pV(x)$ is the pseudo-Voigt function; x and X are variables. Define also: $pV(x)$, x and X.

The structure refinement by the Rietveld method consists of applying the minimum squares method in order to find the structural parameter values to make the calculated intensity and the measured intensity agree in the best possible way. The minimum squares paradigm considers that the best adjustment between a group of N values obtained experimentally $y_i^E(\boldsymbol{x}_i)$ and a model function $f(\boldsymbol{a}, \boldsymbol{x})$, which depends on M refinable parameters a_i, is obtained when the residue χ^2 is minimized, this residue is defined by Eq. (2):

$$\chi^2 = \sum_{i=1}^{N} \frac{\left|y_i^E - f(\boldsymbol{a}, x_i)\right|^2}{\sigma_i^2} \tag{2}$$

where the vector $\boldsymbol{a}$ represents the parameters to be refined, which are its components. This function has an important statistical significance. It is possible to show that finding the minimum value for $\boldsymbol{\chi^2}$ is equivalent to finding the refined values of the parameters for which there is a higher probability of the model function $\boldsymbol{f}(\boldsymbol{a}, \boldsymbol{x}_i)$ to coincide with the experimental data $\boldsymbol{y_i^E}$ [43].

The parameters refined by the minimum squares method are divided into two categories: structural parameters are those that measure the characteristics in the sample; the net parameters and the instrumental parameters are those which do not depend on the characteristics of the sample but on the experimental conditions [44].

It is important to highlight that the refinement must follow a sequence, where the first parameters to be refined using a standard sample are usually the instrumental ones: GW, GV, etc. Right after the structural parameters are adjusted, which are related to the sample: net parameters (*a, b, c*) and, when necessary, the angles of the unit cell (α, β and γ); atomic positions (*x, y, z*), thermal parameters (isotropic or anisotropic) and last, GU and GP which together with GW and GV are parameters for adjusting width to the half-height expressed by the Cagliotti formula shown in Eq. (3): [45].

Table 3 Terms used by the software GSAS

Acronym	Description
GU, GV, GW, GP	Coefficients in the Cagliotti formula (modified by Scherrer enlargement) from the Gaussian component for the peak width. Where GV and GW are related to the enlargement related to the equipment and GP and GU are related to the enlargement of the crystallite size itself
LX	Coefficient from the Lorentzian component for peak width by the isotropic size of the crystallite
Sfec and ptec	Coefficients of the Lorentzian width, but are used only for anisotropic enlargement. Stec is associated with the component Y and ptec with the component X
Uisos	Atomic dislocations (Uisos)—thermal vibration parameters
S/L and H/L	Geometric terms that describe peak enlargement at low angles, in general $2\theta < 15°$, with CuKα radiation (and also for the enlargement of peaks at high angles $2\theta > 165°$). These terms may be calculated by dividing the width of the diverging and receptive slots by the diffractometer radius. These terms are generally the same and must be fixed for a specific (known) group of slots and diffractometer radius, that is, not for instrumental parameters
Trns	Correction for sample transparency in the Bragg-Brentano geometry. It is the inverse of the absorption effect and for the Bragg-Brentano geometry it is zero for high absorbing samples and different from zero for the low or intermediate absorbing samples
Shft	Correction in the peak position for the vertical displacement of the sample in the Bragg-Brentano geometry. It depends highly on the coupling of the sample to the diffractometer, so special care must be taken to prevent this sort of mistake
Eta	mixed factor Gaussian-Lorentzian
SXXX, SYYY, and SZZZ	Lorentzian anisotropic enlargement factors of microtension

$$H_k^2 = U \tan^2 \theta_k + V \tan \theta_k + W \tag{3}$$

Define V and W, θ_k and U. The definitions of the terms used by the GSAS software used in the refinement according to its manual are described in Table 3.

3.1 Crystallite Size and Microdeformations: Scherrer Equation and Williamson-Hall Graph

In the diffraction peaks enlargement analysis method, it is understood that the total enlargement has three components: crystallites size, residual microdeformations, and instrumental parameters, and each one can be identified separately, as shown by Dehlinger and Kochendörfer [46]. The particle size for each sample was calculated

after the parameters V and W, taken from a standard sample, were refined in order to find the instrumental parameters, which would be used later to nullify the instrumental influence for the peak width calculation. The enlargement of the resulting peak from the residual microdeformation β_s can be expressed by Eq. (4):

$$\beta_s = 4\,\varepsilon\,\tan\theta \tag{4}$$

where ε is the microdeformation and θ is the Bragg angle. The enlargement component originated by the crystallites, β_c, can be expressed by Scherrer's equation (Eq. 5): [47].

$$\beta_c = \frac{k'\lambda}{D\,\cos\theta} \tag{5}$$

where k' is a constant, which depends on the reflection and form of the crystal (which usually has value 1), λ is the radiation wavelength, D is the crystallite size and θ is the Bragg angle. Width at total half-height β already corrected will be the sum of the two equations, represented in Eq. (6):

$$\beta = \beta_s + \beta_c = \frac{k'\lambda}{D\,\cos\theta} + 4\,\varepsilon\,\tan\theta \tag{6}$$

where corrected β is represented by Eq. (7):

$$\beta = \sqrt{\beta_{\text{exp}}^2 - \beta_{\text{inst}}^2} \tag{7}$$

And it will be the same as H_k from the Cagliotti formula. Equation (6) can be rewritten as Eq. (8):

$$\frac{\beta\cos\theta}{\lambda} = \frac{k'}{D} + \frac{4\varepsilon}{\lambda}\sin\theta \tag{8}$$

which will be the equation used to create the Williamson–Hall graph of a first-degree equation, as represented in Fig. 1, where $Y = \frac{\beta\cos\theta}{\lambda}$ and $X = \sin\theta$ and Williamson and Hall [48].

The linear coefficient of the line will provide the value for the size of the crystallite, Eq. (9):

$$D = \frac{1}{b} \tag{9}$$

And the angular coefficient will provide the microdeformations, Eq. (10):

$$\varepsilon = \frac{a\lambda}{4} \tag{10}$$

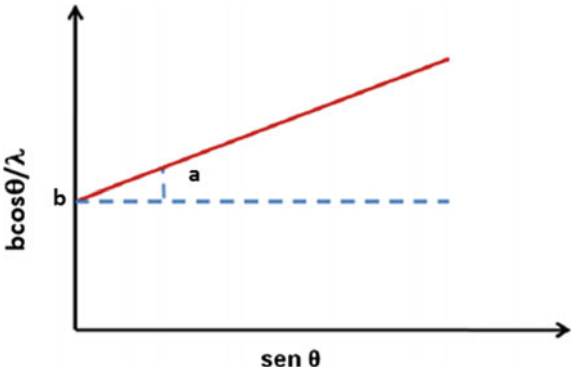

Fig. 1 Representation of Williamson–Hall graph

Properly define/recall parameters Fig. 1a, b. Tension in a material may have two distinct effects over the diffractogram. Due to a uniform effort, compressive or distensive (macrotension), the distances between the atomic plans may become higher or lower, causing the occasional displacement in the position of the peaks.

Uniform efforts are related to the distension and compression simultaneous forces, which result in an enlargement of the diffracted peaks in its original position. This phenomenon, called microtension in crystallites or microdeformation, may be related to different causes: displacements, vacancies, defects, shear planes, thermal expansions, and contractions. Microdeformation may be understood as a relative variation of the net parameter or the interplanar distance caused by the effects mentioned above.

4 Ultrasonometry of the Calcaneus

A great number of comparative studies evaluate the relation between the quantitative ultrasonometry (QU) and the BMD measured by the gold standard dual-energy X-ray absorption (DEXA). QU values may reflect bone density or its architecture or even other bone properties besides density. Previous studies have shown a good relationship between the QU measured in the calcaneus and the BMD also measured in the calcaneus by DEXA, but a poorer correlation between the QU measured in the calcaneus and the BMD from other parts. However, despite the low correlation with other parts of the skeleton, QU proved to be a valid tool for predicting osteoporotic fractures, independent from associations with bone density. The calcaneus is the most popular part for many reasons: It is formed by 90% trabecular bone, having higher bone remodeling than the cortical bone due to the surface/volume reason; it is accessible, the lateral surfaces are relatively plain and parallel, reducing repositioning errors [49–57].

The bone ultrasonometry is based in the determination of the parameters related to two properties that are modified after passing through the material: the bone ultrasound attenuation (BUA) and the apparent speed of wave propagation or speed of sound (SOS), which may be evaluated in different regions such as the tibia, metacarpus, calcaneus, and phalanges [58].

The BUA is based on the loss of energy to the environment, and it includes many variables such as absorption, spreading, diffraction, refraction, and conversion [59, 60].

In commercial apparatus, speed measurements are taken by transmission methods, in which a transducer acts as a transmitter and a second one as a receptor, applied to quantitative measures of bone density. In this method, the speed of the ultrasound in the medium can be calculated by dividing the distance by the corresponding time. In our case, quantitative measures were made in the calcaneus by the use of the transmission method and, for calculating speed, the speed in time of flight (TOF) method, with a fixed separation of the transducers (axial method).

$$\text{speed TOF} = \frac{x V_w}{x - (\Delta t V_w)} \tag{11}$$

In this equation, x is the thickness of the calcaneus including soft tissue, V_w is the speed of the ultrasound in water, and Δt is the difference in time of transit with and without the sample.

5 Materials and Methods

5.1 Ethical Aspects

Sample collection followed the procedures established and approved by the research protocol number 4408/11 of the Research Ethics Committee of the Medicine School in the University of São Paulo, as well as the protocol number 336231 of the Research Ethics Committee of the Federal University of São Carlos.

5.2 Materials

Lumbar vertebrae (L1) were surgically removed from human cadavers, three normal, three osteopenic, and three osteoporotic, 12 h post-mortem, in the Clinical Hospital Morgue, in the city of São Paulo.

5.3 Samples Pre-selection

Before the material was collected, the samples were pre-divided into three groups: normal, osteopenic, and osteoporotic, through QU, using the equipment Achilles InSight (GE Medical Systems Lunar). This pre-selection was conducted as the cadavers arrived at the morgue, before the necropsy technicians started the autopsy. Both feet of each cadaver were placed in the equipment, and triple measurements were taken, calculating the average for each foot and the total average.

5.4 Sample Preparation and Characterization

At the Institute of Orthopedics and Traumatology (IOT) in the Clinical Hospital (CH) in the city of São Paulo, more specifically in the biomechanics laboratory, the samples were extracted axially from vertebral frozen corpses using a trephine drill after the surgical procedure of dissection, and they were standardized in cylindrical format of (10 × 20) mm. Bone marrow was extracted by a washing process, and the sample was kept humid with serum, frozen at −20 °C.

The samples analyzed by MEV (Zeiss Leo 40—Cambridge, England) at the São Carlos Chemistry Institute had no bone marrow and were dried in a cylindrical shape of (5 × 10) mm, and covered with carbon and gold (approximately 20 nm).

5.5 DRX and Rietveld Method Parameters

Powder DRX has a potency of 40 kV and 40 mA, copper radiation $k - \alpha$, and wavelength $\lambda = 1.54056$ Å. The samples were analyzed at an angle of $\theta/2\theta$ of 20 at 70°, pace of 0.02° of 10 s each, followed by the use of the software EVA for the search match.

The diffractograms obtained by the DRX were refined by the Rietveld method through the software GSAS using the interface EXPGUI. The program ConvX was used to convert the data into a format accepted by the GSAS and the ICSD in order to obtain the file.cif (database standard diffractogram) of hydroxyapatite. A quartz standard was used to calibrate the software to the equipment, refining unit cells, atomic displacements (Uisos), scale factor, background radiation, shft, GW, GV, GU, LX, S/L, and H/L. In order to refine the diffractograms, the shifted Chebyshev function was used with ten terms to consider the anisotropy of the bone (Fig. 2) and the unit cell (Fig. 3), the atomic displacements (Uisos) (Fig. 3), the scale factor (Fig. 4), the background radiation (Fig. 2), the shft (Fig. 5), the GU (Fig. 5), the GP (Fig. 5), the ptec (Fig. 5), the sfec (Fig. 5), and the LX (Fig. 5) were refined in cycles of 10 (Fig. 6) with Marquardt damping (Fig. 6) equals to 1 and the effects caused by

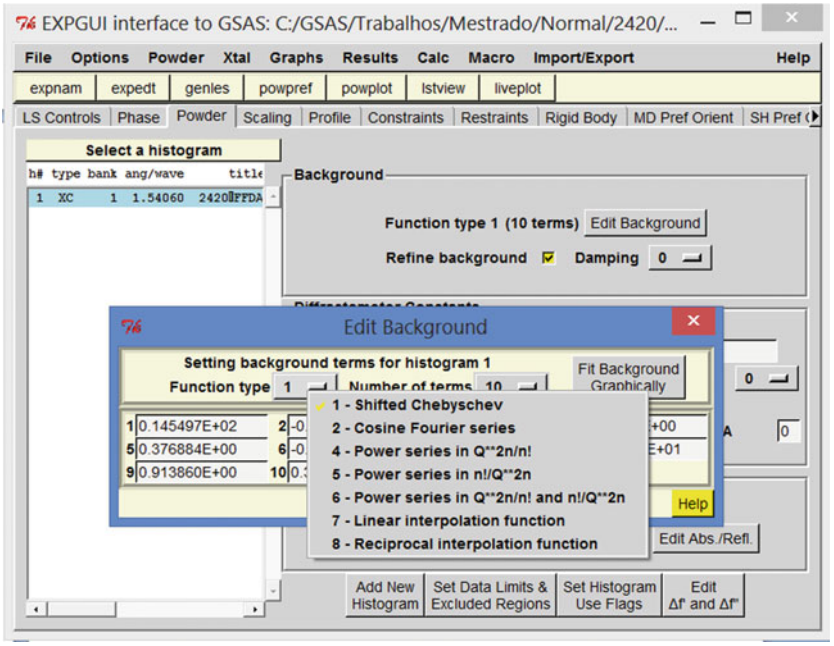

Fig. 2 Use of the function shifted Chebyshev and refinement of background radiation

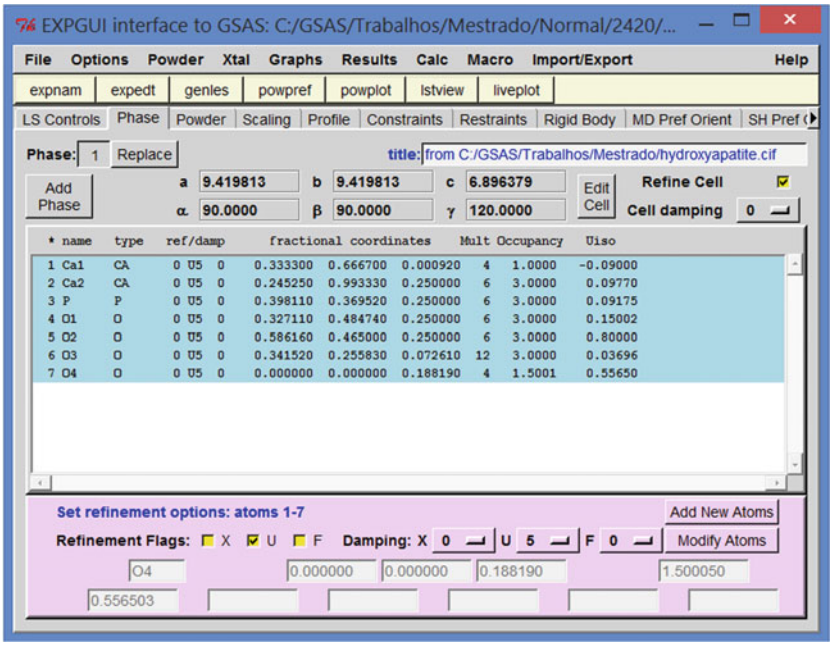

Fig. 3 Refinement of unit cells of the atomic displacements (Uisos)

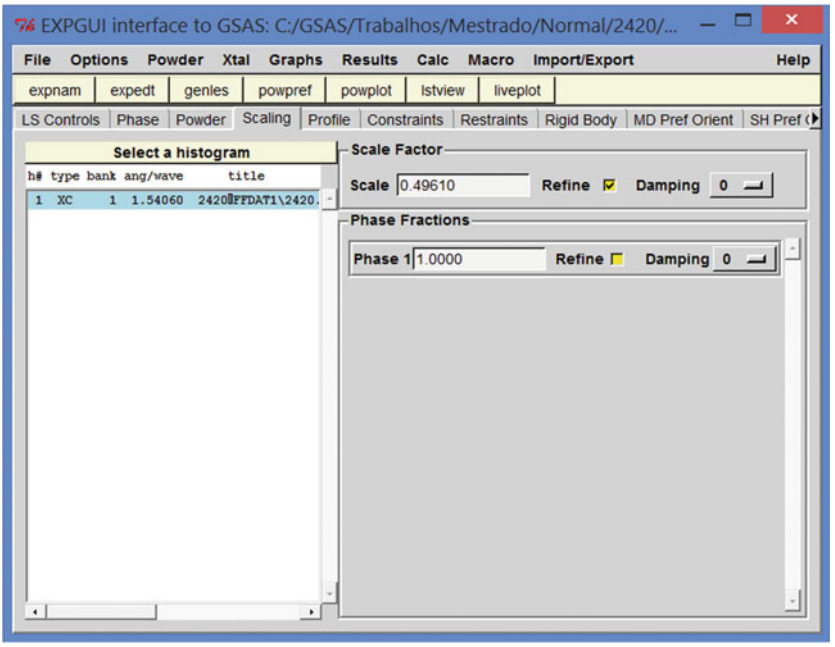

Fig. 4 Scale factor refinement

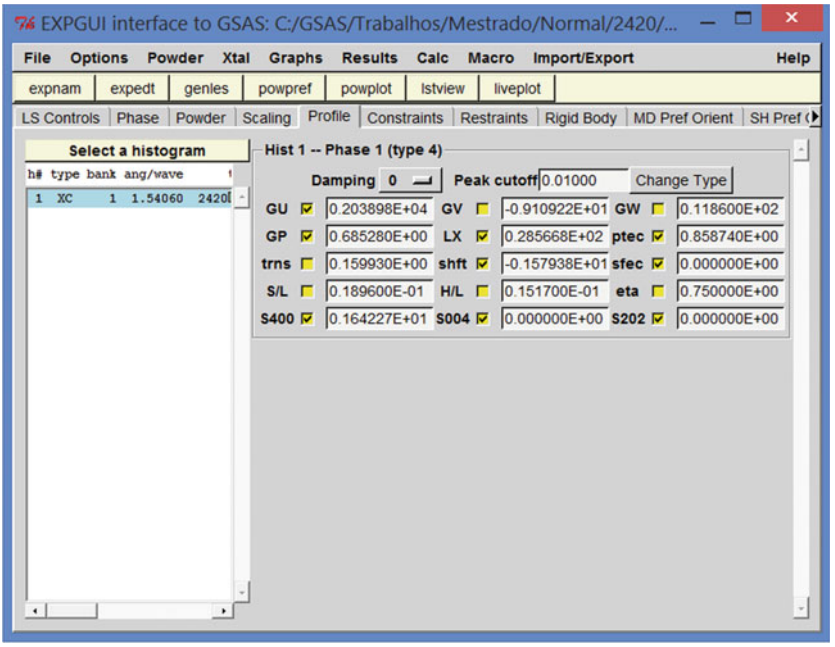

Fig. 5 GU, GP, LX, ptec, shft, sfec, SXXX, SYYY, and SZZZ refinement

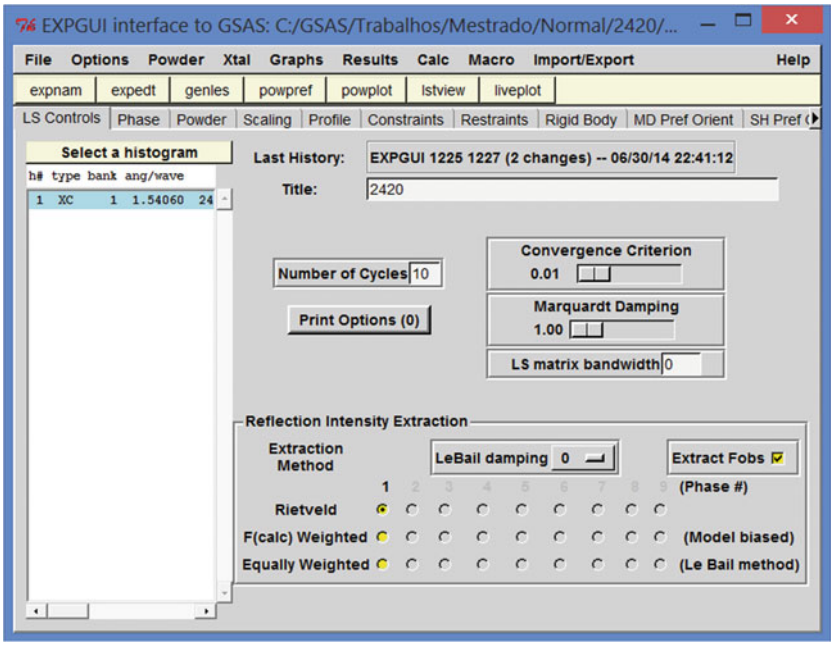

Fig. 6 Marquardt damping use equals 1 in cycles of 10

the preferred orientation were corrected by the use of the March–Dollase model for the planes h k l (2 1 1), (1 2 1), and (1 1 2) (Fig. 7).

6 Results and Discussion

6.1 Ultrasonometry Analysis

Information from the cadaver was collected from the city morgue regarding the age, height, and weight and with the equipment Achilles InSight (GE Medical Systems Lunar), quantitative data in measures of three was obtained, where the average T-score is represented according to Table 4.

These values of T-score represent an indication of the clinical condition of the individuals between 64 and 86 years of age, serving as a reference to separate and correlate the groups, since the T-score relates only to the BMD. However, with further analysis the ultrasonometry prediction was confirmed.

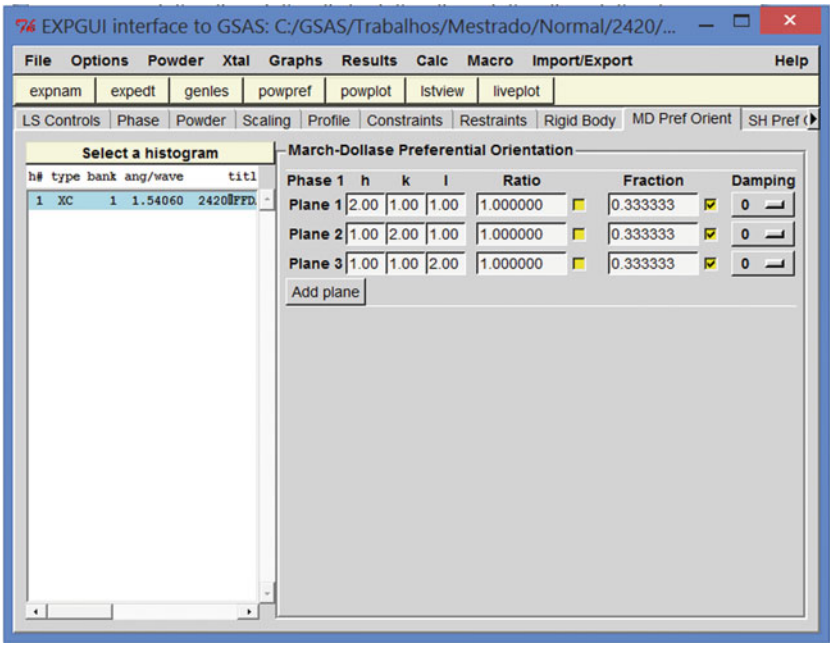

Fig. 7 Correction of the effects caused by preferred orientation using the March–Dollase method in the planes (hkl) equals to (2 1 1), (1 2 1), and (1 1 2)

Table 4 Group classification by the analysis of ultrasonometry of the calcaneus [70]

Group	Age	Height (M)	Weight (Kg)	T-score
Normal 1	67	1.69	46	−0.067
Normal 2	64	1.73	72.2	0.383
Normal 3	81	1.54	45	−0.183
Osteopenic 1	68	1.63	42	−1.383
Osteopenic 2	85	1.75	56	−1.517
Osteopenic 3	82	1.78	70	−1.333
Osteoporotic 1	86	1.61	42	−2.767
Osteoporotic 2	79	1.39	25.4	−2.883
Osteoporotic 3	68	1.7	84	−2.750

This table is reproduced with permissions from Elsevier

6.2 Scanning Electron Microscopy (SEM)

A relation between cracks, fractures, trabecular density with or without plaque formation, connectivity, and the sizes of the pores in the three groups was observed. One normal, one osteopenic, and one osteoporotic were selected. For normal bones

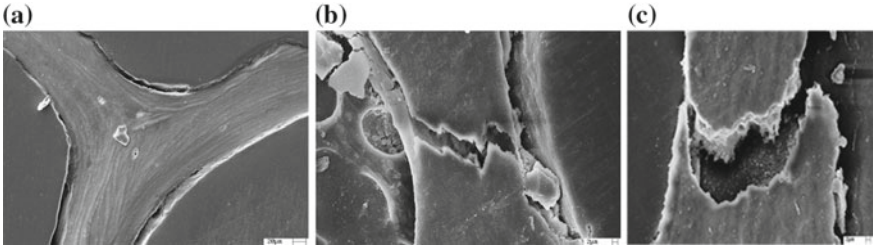

Fig. 8 Scanning electron microscopy of the trabecular bone in human vertebral fixed by epoxy resin and polished: **a** Normal (700 times); **b** Osteopenic (3000 times); **c** Osteoporotic (3000 times)

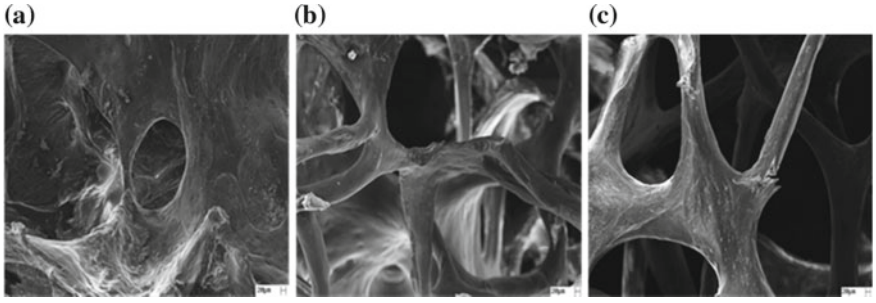

Fig. 9 Scanning electron microscopy of human vertebrae trabecular bone (300 times): **a** Normal; **b** Osteopenic; **c** Osteoporotic

(Figs. 8a and 9a), the microarchitecture was formed by rounded regular pores, with higher connectivity, trabecular number, and the presence of thick and well-organized plaques.

In osteopenic bones (Figs. 8b and 9b), the existence of fragile fractures caused by axial or shear loads, the thinning of the trabeculae and the inexistence of plaque connections were observed. Finally, in bones considered osteoporotic (Figs. 8c and 9c), cracks and fractures with higher irregularity, low connectivity, thinning of the trabeculae and microarchitecture deterioration were observed.

6.3 Dispersive Energy Spectroscopy (DES)

The values found for the phosphorous and calcium proportions are represented in Table 5 and also in Fig. 10.

The Ca/P proportion is higher for normal bones, and the higher the Ca/P proportion, until a certain critical point, the lower the tendency for rupture to take place as seen by Fountos et al. [61] and Kourkoumelis et al. [62] due to probable calcium ions replacements [63], lowering its quantity and increasing the disorganization of

Table 5 Calcium and phosphorous proportions in the 3 stages of the bone

	Normal	Osteopenic	Osteoporotic
Sample 1	1.91	1.80	1.68
Sample 2	2.13	1.80	1.73
Sample 3	2.03	1.82	1.78
Average	2.02	1.81	1.73
Standard deviation	0.11	0.01	0.05

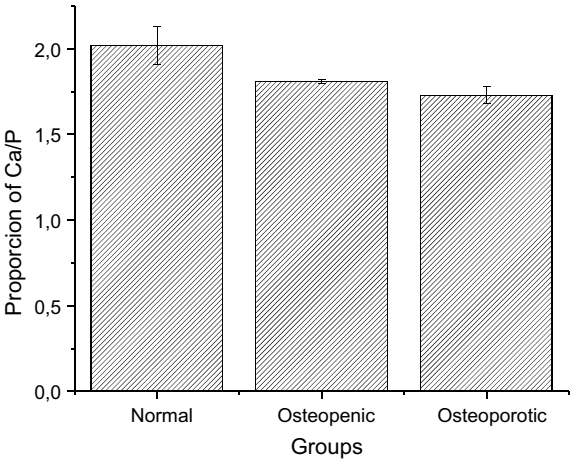

Fig. 10 Calcium and phosphorous proportions in each group

the unit cells in osteopenic and osteoporotic bones. This loss makes the boneless rigid [64, 65], which was confirmed by our microhardness tests, and the disorganization probably caused an increase in microdeformations [61–65].

6.4 Microhardness (HK)

The values analyzed for Knoop microhardness (HK) are presented in Tables 6, 7, and 8 and also in Fig. 11.

Normal bone samples had an average result of 30.27 and standard deviation of 0.36, resulting in 30.27 ± 0.36 HK.

Table 6 Normal sample measurements

Sample	Measure 1	Measure 2	Measure 3	Average
1	30.7	30.7	30.6	30.67
2	28.2	28.8	32.9	29.97
3	30.1	33.9	26.5	30.17

Table 7 Osteopenic samples measurements

Sample	Measure 1	Measure 2	Measure 3	Average
1	26.8	27.9	24	26.23
2	27.3	26.9	23.3	25.83
3	28.9	26.6	24.4	26.63

Table 8 Osteoporotic samples measurements

Samples	Measure 1	Measure 2	Measure 3	Average
1	22	23.2	20.4	21.87
2	23.4	22	19.4	21.6
3	20.3	20.9	19.4	20.2

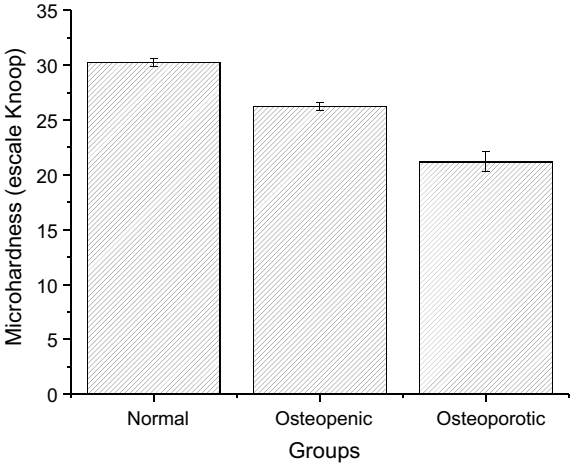

Fig. 11 Microhardness in the Knoop scale for each group

The osteopenic samples in number of three resulted in an average of 26.23 with a standard deviation of 0.440, resulting in 26.23 ± 0.40 HK.

The osteoporotic samples resulted in an average of 21.22 with a standard deviation of $0.89 = 21.22 \pm 0.89$ HK.

The averages and their respective standard deviations are presented in Fig. 11.

It was observed that osteoporotic bones correspond to lower values of microhardness when compared to the normal ones, corroborating the studies of Li et al. [66], Moran et al. [67], and Boivin et al. [68]. The higher the microhardness value, the bigger the resistance to deformation, according to Ferrante [69], which agrees with the reality for osteoporotic bones, that suffer fractures more easily [1, 66–69].

6.5 X-Ray Diffractometry (XRD) and the Rietveld Method

The X-ray diffractometry spectrum of normal, osteopenic, and osteoporotic bones is represented in Fig. 12. It is possible to observe the hydroxyapatite peaks, with no other phase present and hexagonal group $P6_3/m$, typical of hydroxyapatite crystals.

Even though the visual identification is not possible, it is known that normal peaks are larger than osteopenic and osteoporotic ones, once the crystallite sizes are bigger, as a result of Eqs. (3) and (8) [48, 45].

The Bravais solid was produced from the hexagonal three-dimensional structure of the hydroxyapatite through the software Crystal Maker, as shown in Fig. 13. Apparently, the O–H groups are located in the corners of the crystal unit cell, while

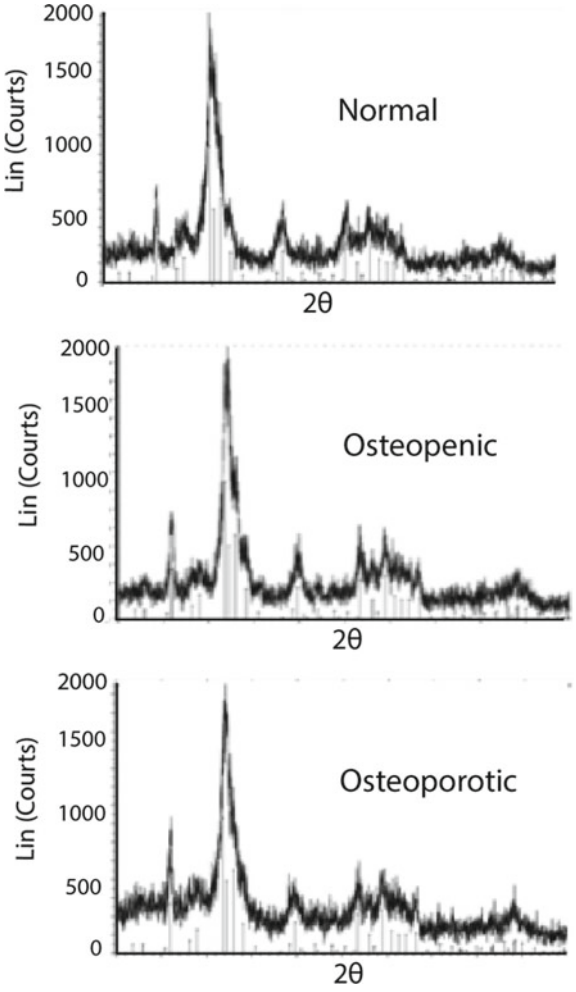

Fig. 12 X-ray diffractometry for each type of bone, from top to bottom; normal, osteopenic, and osteoporotic

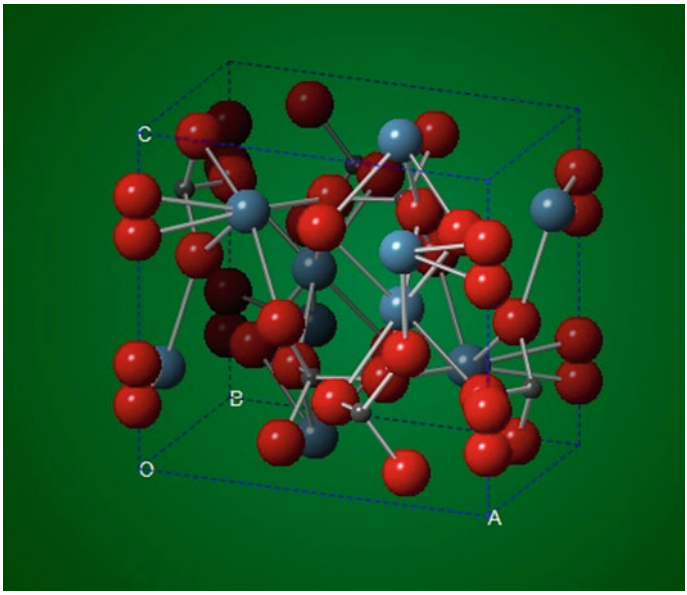

Fig. 13 Crystalline structure of the bone, where O = red, Ca = blue, and P = gray

the Ca, O, and P atoms are located inside the volume, where $a = b \neq c$, with angles $\alpha = \beta = 90°$ and $\gamma = 120°$.

Through the Rietveld method, it was possible to find the sizes of the crystallites, as shown in Table 9 and in Fig. 14.

Microdeformations were also analyzed, as shown in Table 10 and Fig. 15.

Normal bones were found with crystallite sizes bigger than the osteopenic and osteoporotic ones, and the relative variation of the net parameter or interplanar distance caused by the defects (microdeformation), different from the crystallite size, has a lower average for normal bones, when compared to osteopenic and osteoporotic ones. A possible explanation is the increase in microdeformation (disorder) takes place because for the osteoporotic bones there will be a lower exchange of random ions; for the same way, the unbalancing of bone remodeling takes place due to fractures inherent to the aging process, and there is also the addition of different ions to the unit cell. Due to the increase of the disorder in the crystallite and knowing from the literature that a preference for ions with a smaller atomic ratio, it is understood that there will be a decrease in crystallite size. Once it decreases, there is the

Table 9 Crystallite size for each group

Group	Crystallite size (Å)	Standard deviation
Normal	669.34	27.70
Osteopenic	467.38	65.99
Osteoporotic	213.01	86.00

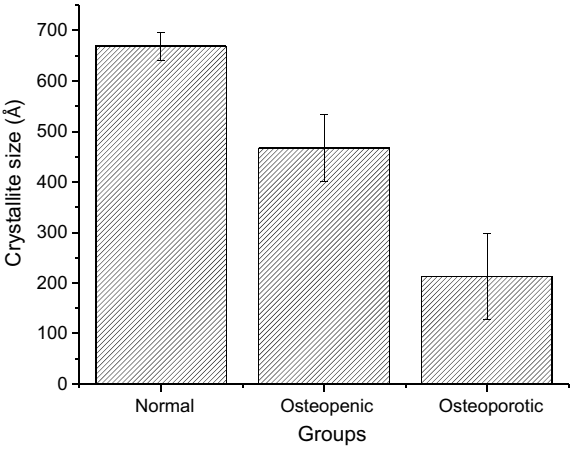

Fig. 14 Crystallite size for the different groups

Table 10 Microdeformation for each group

Group	Microdeformation	Standard Deviation
Normal	5.41	1.58
Osteopenic	11.48	1.57
Osteoporotic	16.88	1.42

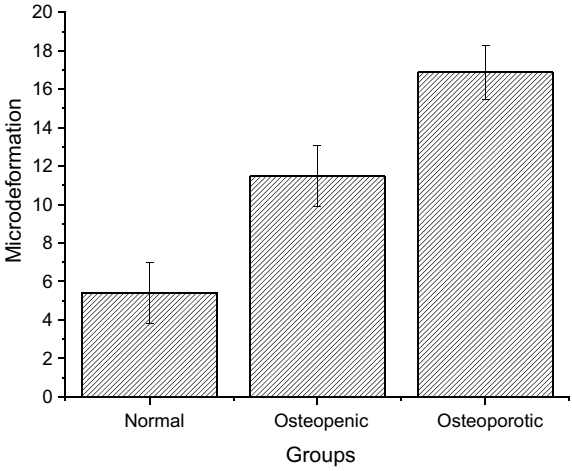

Fig. 15 Microdeformation for each group

possibility of crystallites becoming more compact, which will, once more, increase microdeformation, that also measures the internal tension or the residual tension in the crystallite.

7 Conclusion

The bone microarchitecture of dried trabecular bones vertebrae could be evaluated by the methods: scanning electron microscopy, EDS, microhardness and X-ray diffractometry with the Rietveld refinement method. The microstructural characterization of hydroxyapatite crystals in dried trabecular bones allowed for the identification of the three types of bones (normal, osteopenic, and osteoporotic) and to complement the evaluation and detection of osteoporosis with emphasis on bone quality.

References

1. N.I.H. (2013) National Institute of Arthritis and Muscoloskeletal and Skin Deseases. Consensus statement—osteoporosis prevention, diagnosis, and therapy
2. Bouxsein M (2003) Bone quality: where do we go from here? Osteoporosis Int 14(5):118–127. 9 Jan 2003. ISSN 0937-941X. Available at: http://dx.doi.org/10.1007/s00198-003-1489-x
3. Deborah M, Olof J, Hans W (1996) Meta-analysis of how well measures of bone mineral density predict occurrence of osteoporotic fractures. BMJ 312
4. Kleerekoper M, Balena R (1991) Fluorides and Osteoporosis. Ann Rev Nutr 11(1):309–324. 01 July 1991. ISSN 0199-9885. Available at: http://dx.doi.org/10.1146/annurev.nu.11.070191.001521. Consulted on: 16 July 1991
5. Miller P (2006) Guidelines for the diagnosis of osteoporosis: T-scores vs fractures. Rev Endocr Metab Disord 7(1–2):75–89. 01 June 2006. ISSN 1389-9155. Available at: http://dx.doi.org/10.1007/s11154-006-9006-0
6. Qu Y et al (2005) The effect of raloxifene therapy on the risk of new clinical vertebral fractures at three and six months: a secondary analysis of the MORE trial. Curr Med Res Opin 21(12):1955–1959. 01 Dec 2005. ISSN 0300-7995. Available at: http://informahealthcare.com/doi/abs/10.1185/030079905X75032. Consulted on: 16 July 2013
7. Genant HK, Jiang Y (2006) Advanced imaging assessment of bone quality. Ann NY Acad Sci 1068(1):410–428. ISSN 1749-6632. Available at: http://dx.doi.org/10.1196/annals.1346.038
8. Gourion-Arsiquaud S et al (2009) Use of FTIR spectroscopic imaging to identify parameters associated with fragility fracture. J Bone Miner Res 24(9):1565–1571. ISSN 1523-4681. Available at: http://dx.doi.org/10.1359/jbmr.090414
9. Licata A (2009) Bone density vs bone quality: what's a clinician to do? Clevel Clin J Med 76(6):331–336. Available at: http://www.ccjm.org/content/76/6/331.abstract
10. N.O.F. (2013) National Osteoporosis Foundation—Physicians' guide to prevention and treatment of osteoporosis
11. Parfitt AM (2002) Targeted and nontargeted bone remodeling: relationship to basic multicellular unit origination and progression. Bone 30(1):5–7. ISSN 8756-3282. Available at: http://www.sciencedirect.com/science/article/pii/S8756328201006421
12. Qiu S et al (2005) The morphological association between microcracks and osteocyte lacunae in human cortical bone. Bone 37(1):10–15. ISSN 8756-3282. Available at: http://www.sciencedirect.com/science/article/pii/S8756328205000086
13. Van Der Linden JC et al (2001) Mechanical consequences of bone loss in cancellous bone. J Bone Miner Res 16(3):457–465. ISSN 1523-4681. Available at: http://dx.doi.org/10.1359/jbmr.2001.16.3.457
14. Van Der Meulen MCH, Jepsen KJ, Mikić B (2001) Understanding bone strength: size isn't everything. Bone 29(2):101–104. ISSN 8756-3282. Available at: http://www.sciencedirect.com/science/article/pii/S8756328201004914

15. Viguet-Carrin S, Garnero P, Delmas PD (2006) The role of collagen in bone strength. Osteoporosis Int 17(3):319–336. 01 Mar 2006. ISSN 0937-941X. Available at: http://dx.doi.org/10.1007/s00198-005-2035-9
16. W.H.O. (2001) World Health Organization Study Group
17. Zebaze RMD et al (2005) Femoral neck shape and the spatial distribution of its mineral mass varies with its size: clinical and biomechanical implications. Bone 37(2):243–252. ISSN 8756-3282. Available at: http://www.sciencedirect.com/science/article/pii/S8756328205001006
18. Allen MR, Burr DB (2011) Bisphosphonate effects on bone turnover, microdamage, and mechanical properties: what we think we know and what we know that we don't know. Bone 49(1):56–65. ISSN 8756-3282. Available at: http://www.sciencedirect.com/science/article/pii/S8756328210018636
19. Boskey AL, Marks SC. Mineral and matrix alterations in the bones of incisors-absent (ia/ia) osteopetrotic rats. Calcified Tissue International 37(3):287–292. 01 May 1985. ISSN 0171-967X. Available at: http://dx.doi.org/10.1007/BF02554876
20. Cundy T, Reid IR (2012) Paget's disease of bone. Clin Biochem 45(1–2):43–48. ISSN 0009-9120. Available at: http://www.sciencedirect.com/science/article/pii/S0009912011026890
21. Dilworth L et al (2008 Bone and faecal minerals and scanning electron microscopic assessments of femur in rats fed phytic acid extract from sweet potato (Ipomoea batatas). BioMetals 21(2):133–141. 01 Apr 2008. ISSN 0966-0844. Available at: http://dx.doi.org/10.1007/s10534-007-9101-z
22. Fratzl P et al (1996) Effects of sodium fluoride and alendronate on the bone mineral in minipigs: A small-angle X-ray scattering and backscattered electron imaging study. J Bone Miner Res 11(2):248–253. ISSN 1523-4681. Available at: http://dx.doi.org/10.1002/jbmr.5650110214
23. Leventouri T (2006) Synthetic and biological hydroxyapatites: crystal structure questions. Biomaterials 27(18):3339–3342. ISSN 0142-9612. Available at: http://www.sciencedirect.com/science/article/pii/S0142961206001761
24. Marcus R et al (2009) Fundamentals of osteoporosis, 1ª edn. Elsevier, UK. eBook ISBN: 9780123751089
25. Noor A et al (2011) Assessment of microarchitecture and crystal structure of hydroxyapatite in osteoporosis. Univ Med 31(1)
26. Ou-Yang H et al (2001) Infrared microscopic imaging of bone: spatial distribution of CO_3^{2-}. J Bone Miner Res 16(5):893–900. ISSN 1523-4681. Available at: http://dx.doi.org/10.1359/jbmr.2001.16.5.893
27. Saito M, Marumo K (2010) Collagen cross-links as a determinant of bone quality: a possible explanation for bone fragility in aging, osteoporosis, and diabetes mellitus. Osteoporos Int 21(2):195–214. 01 Feb 2010. ISSN 0937-941X. Available at: http://dx.doi.org/10.1007/s00198-009-1066-z
28. Shen Y et al (2009) Postmenopausal women with osteoarthritis and osteoporosis show different ultrastructural characteristics of trabecular bone of the femoral head. BMC Musculoskelet Disord 10(1):35. ISSN 1471–2474. Available at: http://www.biomedcentral.com/1471-2474/10/35
29. Ginebra M-P et al (1999) Modeling of the hydrolysis of α-tricalcium phosphate. J Am Ceram Soc 82(10):2808–2812. ISSN 1551-2916. Available at: http://dx.doi.org/10.1111/j.1151-2916.1999.tb02160.x
30. Klein CPAT et al (1990) Studies of the solubility of different calcium phosphate ceramic particles in vitro. Biomaterials 11(7):509–512. ISSN 0142-9612. Available at: http://www.sciencedirect.com/science/article/pii/014296129090067Z
31. Barrere F et al (2002) Influence of ionic strength and carbonate on the Ca-P coating formation from SBF × 5 solution. Biomaterials 23(9):1921–1930. ISSN 0142-9612. Available at: http://www.sciencedirect.com/science/article/pii/S0142961201003180
32. Raynaud S et al (2002) Calcium phosphate apatite with variable Ca/P atomic ratio I. Synthesis, characterisation and thermal stability of powders. Biomaterials 23(4):1065–1072. ISSN 0142-9612. Available at: http://www.sciencedirect.com/science/article/pii/S0142961201002186

33. Dekker RJ et al (2005) Bone tissue engineering on amorphous carbonated apatite and crystalline octacalcium phosphate-coated titanium discs. Biomaterials 26(25):5231–5239. ISSN 0142-9612. Available at: http://www.sciencedirect.com/science/article/pii/S0142961205001079
34. Hill RJ, Howard CJ (1987) Quantitative phase analysis from neutron powder diffraction data using the Rietveld method. J Appl Crystallogr 20(6):467–474. ISSN 0021-8898. Available at: http://dx.doi.org/10.1107/S0021889887086199
35. Langford JI, Louer D, Scardi P (2000) Effect of a crystallite size distribution on X-ray diffraction line profiles and whole-powder-pattern fitting. J Appl Crystallogr 33(3):964–974. ISSN 0021-8898. Available at: http://dx.doi.org/10.1107/S002188980000460X
36. Pecharsky VK (2009) Fundamentals of powder diffraction and structural characterization of materials, 2nd edn. Springer, Berlin, 744 pp. ISBN 978-0-387-09579-0
37. Rietveld H (1967) Line profiles of neutron powder-diffraction peaks for structure refinement. Acta Crystallogr 22(1):151–152. 01 Oct 1967. ISSN 0365-110X. Available at: http://dx.doi.org/10.1107/S0365110X67000234
38. Rietveld HM (1969) A profile refinement method for nuclear and magnetic structures. J Appl Crystallogr 2(2):65–71. 06 Feb 1969. ISSN 0021-8898. Available at: http://dx.doi.org/10.1107/S0021889869006558
39. Young RA, Mackie PE, Von Dreele RB (1977) Application of the pattern-fitting structure-refinement method of X-ray powder diffractometer patterns. J Appl Crystallogr 10(4):262–269. 08 Jan 1977. ISSN 0021-8898. Available at: http://dx.doi.org/10.1107/S0021889877013466
40. Enzo S et al (1988) A profile-fitting procedure for analysis of broadened X-ray diffraction peaks. I. Methodology. J Appl Crystallogr 21(5):536–542. 10 Jan 1988. ISSN 0021-8898. Available at: http://dx.doi.org/10.1107/S0021889888006612
41. Louer D, Langford JI (1988) Peak shape and resolution in conventional diffractometry with monochromatic X-rays. J Appl Crystallogr 21(5):430–437. 10 Jan 1988. ISSN 0021-8898. Available at: http://dx.doi.org/10.1107/S002188988800411X
42. Madsen IC, Hill RJ (1988) Effect of divergence and receiving slit dimensions on peak profile parameters in Rietveld analysis of X-ray diffractometer data. J Appl Crystallogr 21(5):398–405. 10 Jan 1988. ISSN 0021-8898. Available at: http://dx.doi.org/10.1107/S0021889888003474
43. Press WH, Teukolsky SA (2007) Numerical recipes in C++, 3rd edn. The Art of Scientific Programming Cambridge University Press, 1256 pp. ISBN: 978-0521880688
44. Teixeira EM (2013) Particle size refinement and microstrain polycrystalline samples by X-ray diffraction profiles using kinetic and dynamic theories. 46 (Physics Bachelor). Department of Physics, Federal University of Ceará, Fortaleza
45. Caglioti G, Paoletti A, Ricci FP (1958) Choice of collimators for a crystal spectrometer for neutron diffraction. Nucl Instrum 3(4):223–228. ISSN 0369-643X. Available at: http://www.sciencedirect.com/science/article/pii/0369643X5890029X
46. Dehlinger U, Kochendörfer A (1939) Linienverbreiterung von verformten Metallen. Zeitschrift Für Kristallographie. Cryst Mater 101(1–6). https://doi.org/10.1524/zkri.1939.101.1.134
47. Azàroff LV (1968) Elements of x-ray crystallography. McGraw-Hill Book Company, New York
48. Williamson GK, Hall WH (1953) X-ray line broadening from filed aluminium and wolfram. Acta Metallurgica 1(1):22–31. ISSN 0001-6160. Available at: http://www.sciencedirect.com/science/article/pii/0001616053900066
49. Aguado F et al (1996) Behavior of bone mass measurements—dual energy X-ray absorptiometry total body bone mineral content, ultrasound bone velocity, and computed metacarpal radiogrammetry, with age, gonadal status, and weight in healthy women. Investigative Radiol 31(4):218-222. ISSN 0020-9996. Available at: Go to ISI: WOS:A1996UE33000006
50. Faulkner KG et al (1994) Quantitative ultrasound of the heel—correlation with densitometric measurements at different skeletal sites. Osteoporos Int 4(1):42–47. ISSN 0937-941X. Available at: Go to ISI: WOS:A1994MT96000008
51. Hans D et al (1996) Ultrasonographic heel measurements to predict hip fracture in elderly women: the EPIDOS prospective study. Lancet 348(9026):511–514. 24 Aug 1996. ISSN 0140-6736. Available at: Go to ISI : WOS:A1996VD42700011

52. Kwok T et al (2012) Predictive values of calcaneal quantitative ultrasound and dual energy X-ray absorptiometry for non-vertebral fracture in older men: results from the MrOS study (Hong Kong). Osteoporos Int 23(3):1001–1006. ISSN 0937-941X. Available at: Go to ISI: WOS:000300251200023
53. Ross P et al (1995) Predicting vertebral deformity using bone densitometry at various skeletal sites and calcaneus ultrasound. Bone 16(3):325–332. ISSN 8756-3282. Available at: Go to ISI: WOS:A1995RB63800007
54. Salamone LM et al (1994) Comparison of broad-band ultrasound attenuation to single x-ray absorptiometry measurements at the calcaneus in postmenopausal women. Calcif Tissue Int 54(2):87–90. ISSN 0171-967X. Available at: Go to ISI: WOS:A1994MT40200002
55. Turner CH et al (1995) Calcaneal ultrasonic measurements discriminate hip fracture independently of bone mass. Osteoporos Int 5(2):130–135. ISSN 0937-941X. Available at: Go to ISI: WOS:A1995QM68000010
56. Waud CE, Lew R, Baran DT (1992) The relationship between ultrasound and densitometric measurements of bone mass at the calcaneus in women. Calcif Tissue Int 51(6):415–418. ISSN 0171-967X. Available at: Go to ISI: WOS:A1992JY74200004
57. Yeap SS et al (1998) The relationship between bone mineral density and ultrasound in postmenopausal and osteoporotic women. Osteoporos Int 8(2):141–146. ISSN 0937-941X. Available at: Go to ISI: WOS:000078768900008
58. Cortet B et al (2004) Does quantitative ultrasound of bone reflect more bone mineral density than bone microarchitecture? Calcif Tissue Int 74(1):60–67. 01 Jan 2004. ISSN 0171-967X. Available at: http://dx.doi.org/10.1007/s00223-002-2113-3
59. Webb S (2012) The physics of medical imaging, 2 edn. CRC Press is an imprint of Taylor & Francis Group, Boca Raton. ISBN-13: 978-1-4665-6895-2 (eBook—PDF)
60. Njeh CF et al (1999) Quantitative ultrasound assessment of osteoporosis and bone status. London Martin Dunitz. ISBN: 1-85317-679-6, 420 pp. doi: https://doi.org/10.1016/S0301-5629(00)00280-5
61. Fountos G et al (1998) The effects of inflammation-mediated osteoporosis (IMO) on the skeletal Ca/P ratio and on the structure of rabbit bone and skin collagen. Appl Radiat Isotopes 49(5–6):657–659. ISSN 0969-8043. Available at: http://www.biomedsearch.com/nih/effects-inflammation-mediated-osteoporosis-IMO/9569570.html
62. Kourkoumelis N, Balatsoukas I, Tzaphlidou M (2012) Ca/P concentration ratio at different sites of normal and osteoporotic rabbit bones evaluated by Auger and energy dispersive X-ray spectroscopy. J Biol Phys 38(2):279–291. ISSN 0092-0606. Available at: http://dx.doi.org/10.1007/s10867-011-9247-3
63. Costa ACFM et al (2009) Hydroxyapatite: collection, characterization and applications. Eletr J Mater Proces 4(3):10
64. Garnet LP, Hiatt JL (2003) Treaty of histology. 2. Rio de Janeiro: Guanabara Koogan. ISBN: 8527708132
65. Junqueira LC, Carneiro J (2008) In: de Janeiro R (ed) Basic histology, 11th edn. Guanabara Koogan. ISBN: 9788527731812
66. Li B, Aspden RM (1997) Mechanical and material properties of the subchondral bone plate from the femoral head of patients with osteoarthritis or osteoporosis. Ann Rheum Dis 56(4):247–254, 1997. Available at: http://ard.bmj.com/content/56/4/247.abstract
67. Moran P et al (2007) Preliminary work on the development of a novel detection method for osteoporosis. J Mater Sci Mater Med 18(6):969–974. 01 Jun 2007. ISSN 0957-4530. Available at: http://dx.doi.org/10.1007/s10856-006-0037-6
68. Boivin G et al (2008) The role of mineralization and organic matrix in the microhardness of bone tissue from controls and osteoporotic patients. Bone 43(3):532–538. ISSN 8756-3282. Available at: http://www.sciencedirect.com/science/article/pii/S8756328208002834
69. Ferrante M (1996) Material selection. EDUFSCar, São Carlos
70. Rollo JMDA et al (2015) Assessment of trabecular bones microarchitectures and crystal structure of hydroxyapatite in bone osteoporosis with application of the rietveld method. Procedia Eng 110:8–14. ISSN 1877-7058. https://doi.org/10.1016/j.proeng.2015.07.003